Phase-sensitivity enhancement based on a four-beam nonlinear interferometer

Jiabin Wang,[1] Shengshuai Liu,[1,4,*] and Jietai Jing[1,2,3,†]

[1]*State Key Laboratory of Precision Spectroscopy, Joint Institute of Advanced Science and Technology, School of Physics and Electronic Science, East China Normal University, Shanghai* 200062*, China*

[2]*CAS Center for Excellence in Ultra-intense Laser Science, Shanghai* 201800*, China*

[3]*Collaborative Innovation Center of Extreme Optics, Shanxi University, Taiyuan, Shanxi* 030006*, China*

[4]*Chongqing Key Laboratory of Precision Optics, Chongqing Institute of East China Normal University, Chongqing 401120, China*

(Received 13 February 2023; accepted 12 March 2024; published 15 April 2024)

We propose a different type of nonlinear interferometer, namely, four-beam nonlinear interferometer, which can realize phase-sensitivity enhancement. We compare the phase sensitivity of the four-beam nonlinear interferometer and the corresponding shot-noise limit. Our results demonstrate that the four-beam nonlinear interferometer can achieve a phase-sensitivity enhancement compared with the corresponding shot-noise limit. Moreover, taking the losses into consideration, the phase sensitivity of the four-beam nonlinear interferometer can also beat the corresponding shot-noise limit. Our scheme may find potential applications in multiparameter quantum metrology.

DOI: 10.1103/PhysRevA.109.043710

I. INTRODUCTION

In metrology [1], optical interferometers have been widely utilized for measuring small variations of different physical quantities [2]. However, it was revealed by Caves [3] in 1981 that the sensitivities of traditional optical interferometers are bounded by $1/\sqrt{N_s}$ [shot-noise limit (SNL)], where N_s is the average photon number inside the interferometer [4]. In order to beat such limit, quantum metrology [5–7] was developed by applying the basic principles of quantum physics to metrology. How to improve the performance of the interferometer is a critical task for quantum metrology, resulting in the development of quantum interferometer.

To improve the measurement accuracy of the interferometer, a quantum interferometer can be constructed by injecting different types of quantum states, such as squeezed states [8–11], Fock states [12], and NOON states [13,14]. For example, squeezed states have been used to reduce the noise of the Laser Interferometer Gravitational-Wave Observatory (LIGO) [15,16] and the polarization interferometer [17]. Meanwhile, the performance of an interferometer also depends on detection schemes, such as parity detection [18,19], homodyne detection [20], and intensity detection [21]. Moreover, replacing the linear beam splitters in the Mach-Zehnder interferometer (MZI) [22,23] with parametric amplifiers (PAs) can obtain a quantum-enhanced phase sensitivity. This leads to the birth of SU(1,1) interferometer [24].

Phase sensitivity is crucial for characterizing the performance of an interferometer. It is defined as the uncertainty of phase estimation. Specifically, this physical quantity represents the minimal variation of internal phase that can be detected. It has been demonstrated that SU(1,1) interferometer can achieve quantum enhancement of phase sensitivity [25–34] compared with MZI. Moreover, multiple-beam interference can improve signal-to-noise ratio [35], which is important for improving the sensitivity of an interferometer. In this paper, by introducing four-beam interference into interferometer, we propose a different type of nonlinear interferometer, namely, four-beam nonlinear interferometer (FBNI). We find that FBNI can realize a phase-sensitivity enhancement compared with the corresponding SNL. In addition, we discuss the effect of losses on the phase sensitivity of FBNI.

II. MODEL AND PHASE SENSITIVITY OF FOUR-BEAM NONLINEAR INTERFEROMETER

The schematic of FBNI is shown in Fig. 1. FBNI consists of two four-beam PAs (FBPAs), which are realized by spatially multiplexed four-wave mixing (FWM) processes in hot rubidium vapor cells. We consider a coherent state $|\alpha\rangle_{\text{in}}$ and three vacuum states as inputs of the first FBPA. The red, yellow, and blue beams denote pump, probe, and conjugate beams, respectively. We define $\hat{a}_{\text{in}1}$, $\hat{a}_{\text{in}2}$, $\hat{a}_{\text{in}3}$, $\hat{a}_{\text{in}4}$ as the annihilation operators of the four inputs and $\hat{a}_1$, $\hat{a}_2$, $\hat{a}_3$, $\hat{a}_4$ as the annihilation operators of the outputs from the first FBPA. The two pump beams are symmetrically crossed at the center of the vapor cell in a horizontal plane. The coherent input beam $\hat{a}_{\text{in}3}$ is crossed with pump_1 in a vertical plane. In this way, these three beams intersect at the center of the vapor cell. There are two single-pump FWM processes [36,37] and two dual-pump FWM processes [38,39] in the whole process. First, the conjugate beam $\hat{a}_1$, probe beam $\hat{a}_3$ and pump_1 are depicted on the same black line, representing a conventional single-pump FWM process. In this process, two annihilated photons both come from pump_1, while conjugate beam $\hat{a}_1$ and probe beam $\hat{a}_3$ obtain one photon, respectively. In other words, the interaction between input probe beam $\hat{a}_{\text{in}3}$ and

*Corresponding author: ssliu@lps.ecnu.edu.cn
†Corresponding author: jtjing@phy.ecnu.edu.cn

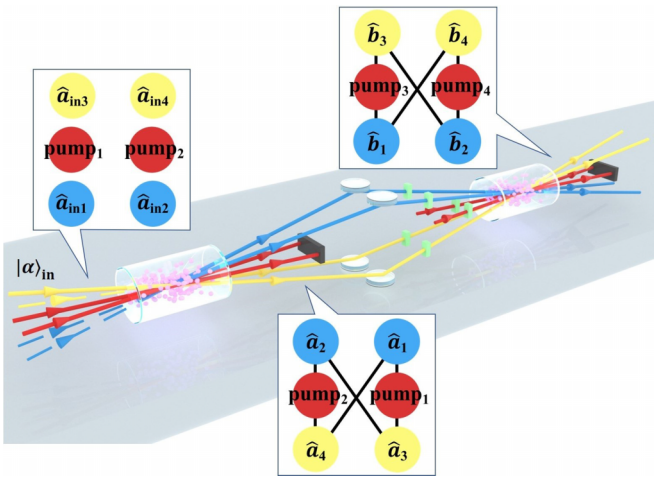

FIG. 1. Schematic for FBNI with two FBPAs. The green boxes are phase shifters. The red, yellow, and blue beams denote the pump, probe, and conjugate beams, respectively. The input conjugate fields $\hat{a}_{in1}$, $\hat{a}_{in2}$ and probe field $\hat{a}_{in4}$ are vacuum fields, while the input probe field $\hat{a}_{in3}$ is a coherent field.

pump$_1$ results in the generation of conjugate beam $\hat{a}_1$ and the amplification of input probe beam $\hat{a}_{in3}$. At the same time, the input probe beam $\hat{a}_{in3}$ also interacts with both pump$_1$ and pump$_2$ simultaneously, initiating a dual-pump FWM process. This process is represented by the black line connecting conjugate beam $\hat{a}_2$ and probe beam $\hat{a}_3$. This black line passes through the midpoint of two pump beams, indicating that the two annihilated photons in the dual-pump FWM process come from both pump beams. As a result of this dual-pump FWM process, conjugate beam $\hat{a}_2$ is generated, and the input probe beam is amplified again. Subsequently, the single-pump FWM process between new conjugate beam $\hat{a}_2$ and pump$_2$ generates the probe beam $\hat{a}_4$. And the dual-pump FWM process between new conjugate beam $\hat{a}_1$ and dual pump beams also generates the probe beam $\hat{a}_4$. Through these FWM processes, one amplified probe beam ($\hat{a}_3$) and three new beams (one new probe beam $\hat{a}_4$ and two new conjugate beams $\hat{a}_1$, $\hat{a}_2$) are obtained. The two pump beams in this FBPA have the same power and beam waist. Under such configuration, the interaction strength of each single-pump FWM process can be regarded as ξ_1, and the interaction strength of each dual-pump FWM process can be regarded as ξ_2. Then, the interaction Hamiltonian of the first FBPA can be given by

$$\hat{H} = i\hbar[\xi_1(\hat{a}_1^\dagger\hat{a}_3^\dagger + \hat{a}_2^\dagger\hat{a}_4^\dagger) + \xi_2(\hat{a}_1^\dagger\hat{a}_4^\dagger + \hat{a}_2^\dagger\hat{a}_3^\dagger)] + \text{H.c.}, \quad (1)$$

where H.c. is the Hermitian conjugate. Thus, the input-output relations of such a FBPA can be given by

$$\begin{aligned}
\hat{a}_1 &= A\hat{a}_{in1} + B\hat{a}_{in2} + C\hat{a}_{in3}^\dagger + D\hat{a}_{in4}^\dagger,\\
\hat{a}_2 &= B\hat{a}_{in1} + A\hat{a}_{in2} + D\hat{a}_{in3}^\dagger + C\hat{a}_{in4}^\dagger,\\
\hat{a}_3^\dagger &= C\hat{a}_{in1} + D\hat{a}_{in2} + A\hat{a}_{in3}^\dagger + B\hat{a}_{in4}^\dagger,\\
\hat{a}_4^\dagger &= D\hat{a}_{in1} + C\hat{a}_{in2} + B\hat{a}_{in3}^\dagger + A\hat{a}_{in4}^\dagger,
\end{aligned} \quad (2)$$

where $A = \sqrt{G_1G_2}$, $B = \sqrt{(G_1-1)(G_2-1)}$, $C = \sqrt{G_2(G_1-1)}$, and $D = \sqrt{G_1(G_2-1)}$. $G_1 = \cosh^2(\xi_1 t)$ is the intensity gain of the single-pump FWM process, and $G_2 = \cosh^2(\xi_2 t)$ is the intensity gain of the dual-pump FWM process. t is the interaction time scale. Then, the four outputs of the first FBPA are sent into the second FBPA simultaneously by using a 4f imaging system and interact with two new pump beams (pump$_3$ and pump$_4$). The second FBPA has the same configuration and intensity gains as the first FBPA. The output fields of the second FBPA process can be given by

$$\begin{aligned}
\hat{b}_1 &= Ae^{i\theta_1}\hat{a}_1 + Be^{i(\phi_1-\phi_2+\theta_2)}\hat{a}_2 + Ce^{i(2\phi_1-\theta_3)}\hat{a}_3^\dagger + De^{i(\phi_1+\phi_2-\theta_4)}\hat{a}_4^\dagger,\\
\hat{b}_2 &= Be^{-i(\phi_1-\phi_2-\theta_1)}\hat{a}_1 + Ae^{i\theta_2}\hat{a}_2 + De^{i(\phi_1+\phi_2-\theta_3)}\hat{a}_3^\dagger + Ce^{i(2\phi_2-\theta_4)}\hat{a}_4^\dagger,\\
\hat{b}_3^\dagger &= Ce^{-i(2\phi_1-\theta_1)}\hat{a}_1 + De^{-i(\phi_1+\phi_2-\theta_2)}\hat{a}_2 + Ae^{-i\theta_3}\hat{a}_3^\dagger + Be^{-i(\phi_1-\phi_2+\theta_4)}\hat{a}_4^\dagger,\\
\hat{b}_4^\dagger &= De^{-i(\phi_1+\phi_2-\theta_1)}\hat{a}_1 + Ce^{-i(2\phi_2-\theta_2)}\hat{a}_2 + Be^{i(\phi_1-\phi_2-\theta_3)}\hat{a}_3^\dagger + Ae^{-i\theta_4}\hat{a}_4^\dagger,
\end{aligned} \quad (3)$$

where ϕ_k ($k = 1, 2$) is the phase of new pump fields. θ_j denotes the phases of the conjugate fields ($j = 1, 2$) and probe fields ($j = 3, 4$). Combining Eqs. (2) and (3), we can obtain the input-output relations of the whole FBNI, which are given in Appendix A.

The phase sensitivity $\Delta\varphi$ of the interferometer can be defined as

$$\Delta\varphi = \sqrt{\frac{\langle(\Delta\hat{N}_{out})^2\rangle}{|\partial\langle\hat{N}_{out}\rangle/\partial\varphi|^2}}, \quad (4)$$

where $\langle(\Delta\hat{N}_{out})^2\rangle = \langle\hat{N}_{out}^2\rangle - \langle\hat{N}_{out}\rangle^2$ and φ is the internal phase of the interferometer. $\langle(\Delta\hat{N}_{out})^2\rangle$ and $\langle\hat{N}_{out}\rangle$ stand for the intensity noise and average intensity of the measured field, respectively. For the above coherent state injected FBNI, direct intensity detection is chosen as the measurement strategy. For simplicity, the phase difference between two pump fields ($\phi_1 - \phi_2$), two conjugate fields ($\theta_1 - \theta_2$), and two probe fields ($\theta_3 - \theta_4$) is set to be equal, which can be realized by phase locking. In this way, the total phase inside FBNI can be expressed as $\varphi = 2\phi_2 - \theta_2 - \theta_4$ [40] [see details in Eq. (A3) and corresponding descriptions in Appendix A]. The phase of $\hat{N}_{out}$ will only depend on φ. Assuming that the number of injected photons $N_{\hat{a}_{in3}} \gg 1$ and intensity gain $G_1 = G_2 = G$, the phase sensitivities of FBNI with different photon number combinations can be obtained. Based on the

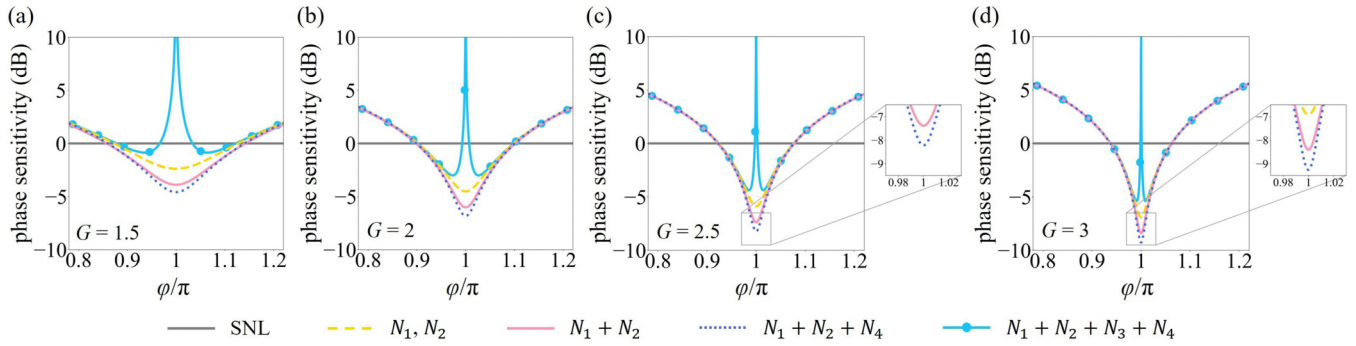

FIG. 2. The phase sensitivities of FBNI with four photon number combinations versus φ in the lossless case with the same internal photon number and $G_1 = G_2 = G$. When (a) $G = 1.5$, (b) $G = 2$, (c) $G = 2.5$, and (d) $G = 3$, the phase sensitivities of FBNI with photon number combinations N_1 (N_2), $N_1 + N_2$, $N_1 + N_2 + N_4$, and $N_1 + N_2 + N_3 + N_4$ are denoted by yellow dashed, pink solid, dark blue dotted, and light blue dot curves, respectively. The corresponding SNLs are denoted by gray straight lines.

analysis provided in Appendix A, it has been concluded that the optimal phase sensitivities are obtained with the photon number combinations of $N_1(N_2)$ for a single port, $N_1 + N_2$ for two ports, $N_1 + N_2 + N_4$ for three ports, and $N_1 + N_2 + N_3 + N_4$ for four ports. The corresponding expressions are given by

$$\begin{aligned}
\Delta\varphi_{N_1} &= \Delta\varphi_{N_2} = \frac{\sqrt{4\varepsilon(2G-1)^2(\cos\varphi+1)^2+(\cos\varphi+1)}}{\sqrt{\varepsilon N_s}|\sin\varphi|},\\
\Delta\varphi_{N_1+N_2} &= \frac{\sqrt{\kappa(\cos\varphi+1)^2+(\cos\varphi+1)}}{\sqrt{2\varepsilon N_s}|\sin\varphi|},\\
\Delta\varphi_{N_1+N_2+N_4} &= \frac{\sqrt{(2G-1)^2[3\varepsilon\kappa(1+3\varepsilon)(\cos\varphi+1)^2+2(\varepsilon+3\varepsilon^2)(\cos\varphi+1)]}}{2\varepsilon(1+3\varepsilon)|\sin\varphi|\sqrt{N_s}},\\
\Delta\varphi_{N_1+N_2+N_3+N_4} &= \frac{\kappa(\cos\varphi+1)+1}{4\varepsilon(2G-1)|\sin\varphi|\sqrt{N_s}},
\end{aligned} \tag{5}$$

where $N_s = (2G-1)^2 N_{\hat{a}_{\text{in}3}}$ is the total internal photon number of FBNI. $\varepsilon = 2G(G-1)$ and $\kappa = 16G(G-1)(2G-1)^2$. As mentioned above, the SNL is given by

$$\Delta\varphi_{\text{SNL}} = 1/\sqrt{N_s}. \tag{6}$$

III. RESULTS AND DISCUSSION

Based on the above equations, we depict the phase sensitivities of each phase point for FBNI with these four photon number combinations and the corresponding SNL in the ideal case without considering the losses. It is well known that the phase sensitivity of an interferometer can be enhanced by increasing the internal photon number. For a fair comparison, the internal photon numbers N_s of FBNI with different photon number combinations are kept equal. As shown in Fig. 2, the yellow dashed, pink solid, dark blue dotted, and light blue dot curves represent the phase sensitivities of FBNI with photon number combinations N_1 (N_2), $N_1 + N_2$, $N_1 + N_2 + N_4$, and $N_1 + N_2 + N_3 + N_4$, respectively. The gray straight lines represent the corresponding SNLs. As shown in Figs. 2(a)–2(d), the phase sensitivities of the FBNI, obtained from photon number combination $N_1 + N_2 + N_4$ (dark blue dotted curves), are better than the phase sensitivities derived from the other combinations at different intensity gain G. In other words, for the same N_s, the photon number combination $N_1 + N_2 + N_4$ is identified as optimal for achieving superior phase sensitivity for FBNI. Therefore, we choose the phase sensitivity obtained by detecting the photon number combination $N_1 + N_2 + N_4$ as the phase sensitivity of FBNI in the following discussion. The phase sensitivity of FBNI increases as the intensity gain G increases from 1.5 to 3, as shown in Figs. 2(a)–2(d). When $G = 2.5$, the phase sensitivity of FBNI at the phase point $\varphi = \pi$ is about 8.22 dB below the SNL, as shown in Fig. 2(c). Compared with the SNL, the FBNI achieves an enhancement of about 8.22 dB with $G = 2.5$.

With the change of internal photon number N_s, the phase-sensitivity scalings on a 10 $\log_{10}$-10 $\log_{10}$ scale are depicted in Fig. 3. The blue solid and gray dashed lines are the phase-sensitivity scalings of FBNI and the corresponding SNL, respectively. With the increase of N_s, the optimal phase sensitivity can be enhanced, as shown in Fig. 3. When $G = 3$ as shown in Fig. 3(d), the phase sensitivity of FBNI (blue solid line) is about 9.26 dB below the SNL (gray dashed line). In other words, FBNI beats the SNL by about 9.26 dB, which clearly shows the ability of FBNI in phase-sensitivity enhancement. More importantly, as shown in Figs. 3(a)–3(d), it can be seen that the higher the intensity gain is, the more the phase sensitivity of FBNI improves.

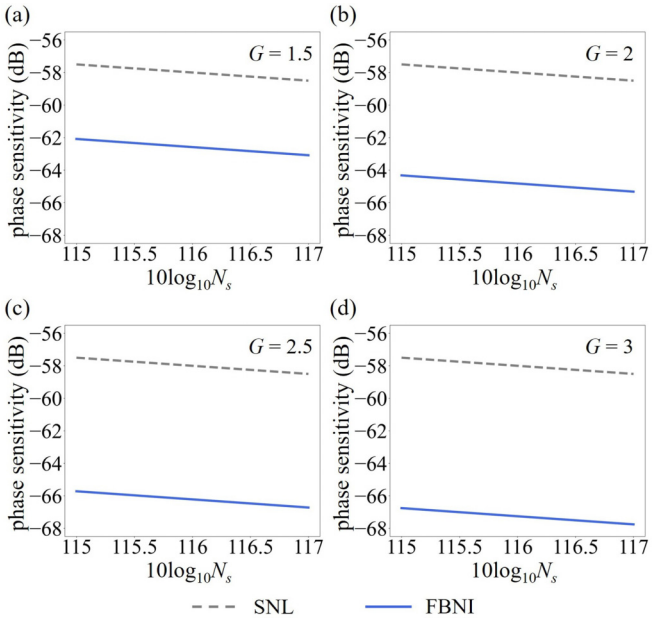

FIG. 3. The phase-sensitivity scalings of FBNI in the ideal case without considering the losses. When (a) $G = 1.5$, (b) $G = 2$, (c) $G = 2.5$, and (d) $G = 3$, the phase sensitivities of FBNI and the corresponding SNLs versus the internal photon number N_s are denoted by blue solid and gray dashed lines, respectively.

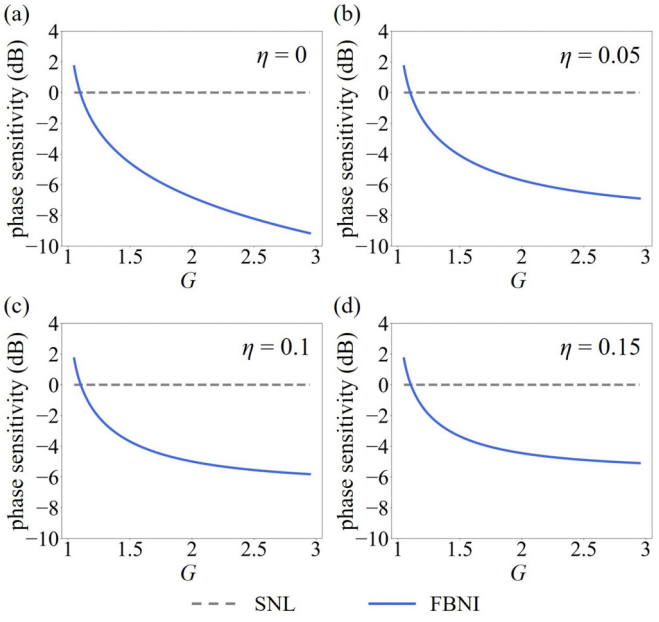

FIG. 4. The phase-sensitivity scalings of FBNI in the case with considering the losses. When (a) $\eta = 0$, (b) $\eta = 0.05$, (c) $\eta = 0.1$, and (d) $\eta = 0.15$, the phase sensitivities of FBNI versus G are denoted by blue solid curves. The phase sensitivities are normalized to the corresponding SNLs, which are denoted by gray dashed lines.

In real experiments, optical losses are unavoidable. The output field after losses can be regarded as a combination of the input field and vacuum field on a beam splitter [41]. Taking the losses of interferometers into account, the phase sensitivity of FBNI with loss ratio η is derived in Appendix B. The corresponding phase-sensitivity scalings are shown in Fig. 4. In order to clearly show the effects of intensity gain and losses on the phase sensitivity, we normalize the phase sensitivities to the SNLs. As shown in Fig. 4, the blue solid curves represent the phase sensitivities of FBNI. The gray dashed lines represent the corresponding SNLs. It can be found that the phase sensitivities increase with the increase of intensity gain, which is consistent with the results in Fig. 2 and Fig. 3. Meanwhile, with the loss ratio η increasing from 0 to 0.15, the phase sensitivities of FBNI become worse, as shown in Figs. 4(a)–4(d). This is due to the fact that the greater the losses are, the more uncorrelated noises [42] will be introduced and amplified, resulting in the deterioration of phase sensitivities. As shown in Figs. 4(a)–4(d), considering the losses, the phase sensitivity of FBNI still beats the SNL. For example, in the case of $\eta = 0.15$ and $G = 2.5$ as shown in Fig. 4(d), the phase sensitivity of FBNI is about 4.89 dB below the SNL. In other words, the FBNI still achieves a phase-sensitivity enhancement of about 4.89 dB with $\eta = 0.15$ and $G = 2.5$.

IV. CONCLUSION

In conclusion, we have proposed a different type of nonlinear interferometer (FBNI) consisting of two identical FBPAs. Such FBNI can achieve an enhancement in terms of phase sensitivity. We compare the phase sensitivities of FBNI and the corresponding SNL. We show that FBNI can achieve a phase-sensitivity enhancement of about 9.26 dB compared to the SNL when $G = 3$. In addition, we discuss the effect of losses on the phase sensitivity of FBNI. Considering the losses, the phase sensitivity of FBNI still beats the SNL. Such a nonlinear interferometer may find potential applications in multiparameter quantum metrology.

ACKNOWLEDGMENTS

This work was funded by the National Natural Science Foundation of China (12225404, 11874155, 91436211, 11374104, and 12174110); Innovation Program of Shanghai Municipal Education Commission (Grant No. 2021-01-07-00-08-E00100); Program of Shanghai Academic Research Leader (22XD1400700); Basic Research Project of Shanghai Science and Technology Commission (20JC1416100); Natural Science Foundation of Shanghai (17ZR1442900); Minhang Leading Talents (201971); Shanghai Sailing Program (21YF1410800); Natural Science Foundation of Chongqing (CSTB2022NSCQ-MSX0893); Shanghai Municipal Science and Technology Major Project (2019SHZDZX01); the 111 project (B12024).

APPENDIX A: PHASE SENSITIVITY OF THE FOUR-BEAM NONLINEAR INTERFEROMETER

FBNI is mainly composed of two FBPAs based on FWM processes in hot rubidium vapor cells. Combining Eqs. (2) and (3) in the main text, the input-output relations of the

whole FBNI can be described as

$$\begin{aligned}
\hat{b}_1 &= [A^2e^{i\theta_1} + B^2e^{i(\phi_1-\phi_2+\theta_2)} + C^2e^{i(2\phi_1-\theta_3)} + D^2e^{i(\phi_1+\phi_2-\theta_4)}]\hat{a}_{\text{in1}} \\
&\quad + [ABe^{i\theta_1} + ABe^{i(\phi_1-\phi_2+\theta_2)} + CDe^{i(2\phi_1-\theta_3)} + CDe^{i(\phi_1+\phi_2-\theta_4)}]\hat{a}_{\text{in2}} \\
&\quad + [ACe^{i\theta_1} + BDe^{i(\phi_1-\phi_2+\theta_2)} + ACe^{i(2\phi_1-\theta_3)} + BDe^{i(\phi_1+\phi_2-\theta_4)}]\hat{a}^\dagger_{\text{in3}} \\
&\quad + [ADe^{i\theta_1} + BCe^{i(\phi_1-\phi_2+\theta_2)} + BCe^{i(2\phi_1-\theta_3)} + ADe^{i(\phi_1+\phi_2-\theta_4)}]\hat{a}^\dagger_{\text{in4}}, \\
\hat{b}_2 &= [ABe^{-i(\phi_1-\phi_2-\theta_1)} + ABe^{i\theta_2} + CDe^{i(\phi_1+\phi_2-\theta_3)} + CDe^{i(2\phi_2-\theta_4)}]\hat{a}_{\text{in1}} \\
&\quad + [B^2e^{-i(\phi_1-\phi_2-\theta_1)} + A^2e^{i\theta_2} + D^2e^{i(\phi_1+\phi_2-\theta_3)} + C^2e^{i(2\phi_2-\theta_4)}]\hat{a}_{\text{in2}} \\
&\quad + [BCe^{-i(\phi_1-\phi_2-\theta_1)} + ADe^{i\theta_2} + ADe^{i(\phi_1+\phi_2-\theta_3)} + BCe^{i(2\phi_2-\theta_4)}]\hat{a}^\dagger_{\text{in3}} \\
&\quad + [BDe^{-i(\phi_1-\phi_2-\theta_1)} + ACe^{i\theta_2} + BDe^{i(\phi_1+\phi_2-\theta_3)} + ACe^{i(2\phi_2-\theta_4)}]\hat{a}^\dagger_{\text{in4}}, \\
\hat{b}^\dagger_3 &= [ACe^{-i(2\phi_1-\theta_1)} + BDe^{-i(\phi_1+\phi_2-\theta_2)} + ACe^{-i\theta_3} + BDe^{-i(\phi_1-\phi_2+\theta_4)}]\hat{a}_{\text{in1}} \\
&\quad + [BCe^{-i(2\phi_1-\theta_1)} + ADe^{-i(\phi_1+\phi_2-\theta_2)} + ADe^{-i\theta_3} + BCe^{-i(\phi_1-\phi_2+\theta_4)}]\hat{a}_{\text{in2}} \\
&\quad + [C^2e^{-i(2\phi_1-\theta_1)} + D^2e^{-i(\phi_1+\phi_2-\theta_2)} + A^2e^{-i\theta_3} + B^2e^{-i(\phi_1-\phi_2+\theta_4)}]\hat{a}^\dagger_{\text{in3}} \\
&\quad + [CDe^{-i(2\phi_1-\theta_1)} + CDe^{-i(\phi_1+\phi_2-\theta_2)} + ABe^{-i\theta_3} + ABe^{-i(\phi_1-\phi_2+\theta_4)}]\hat{a}^\dagger_{\text{in4}}, \\
\hat{b}^\dagger_4 &= [ADe^{-i(\phi_1+\phi_2-\theta_1)} + BCe^{-i(2\phi_2-\theta_2)} + BCe^{i(\phi_1-\phi_2-\theta_3)} + ADe^{-i\theta_4}]\hat{a}_{\text{in1}} \\
&\quad + [BDe^{-i(\phi_1+\phi_2-\theta_1)} + ACe^{-i(2\phi_2-\theta_2)} + BDe^{i(\phi_1-\phi_2-\theta_3)} + ACe^{-i\theta_4}]\hat{a}_{\text{in2}} \\
&\quad + [CDe^{-i(\phi_1+\phi_2-\theta_1)} + CDe^{-i(2\phi_2-\theta_2)} + ABe^{i(\phi_1-\phi_2-\theta_3)} + ABe^{-i\theta_4}]\hat{a}^\dagger_{\text{in3}} \\
&\quad + [D^2e^{-i(\phi_1+\phi_2-\theta_1)} + C^2e^{-i(2\phi_2-\theta_2)} + B^2e^{i(\phi_1-\phi_2-\theta_3)} + A^2e^{-i\theta_4}]\hat{a}^\dagger_{\text{in4}},
\end{aligned} \tag{A1}$$

where $A = \sqrt{G_1G_2}$, $B = \sqrt{(G_1-1)(G_2-1)}$, $C = \sqrt{G_2(G_1-1)}$, and $D = \sqrt{G_1(G_2-1)}$. $G_1 = \cosh^2(\xi_1 t)$ is the intensity gain of the single-pump FWM process, and $G_2 = \cosh^2(\xi_2 t)$ is the intensity gain of the dual-pump FWM process. t is the interaction time scale. Together with the error-propagation analysis [43], assuming that the number of injected photons $N_{\hat{a}_{\text{in3}}} \gg 1$, the intensity noise of the measured field $\hat{b}_1$ can be approximated as

$$\begin{aligned}
\langle(\Delta\hat{N}_1)^2\rangle \approx\ & [2A^2C^2 + 2B^2D^2 + 2A^2C^2\cos(2\phi_1-\theta_1-\theta_3) + 2B^2D^2\cos(2\phi_2-\theta_2-\theta_4) \\
& + 2ABCD\cos(\phi_1+\phi_2-\theta_1-\theta_4) + 2ABCD\cos(\phi_1+\phi_2-\theta_2-\theta_3) \\
& + 2ABCD\cos(\phi_1-\phi_2-\theta_1+\theta_2) + 2ABCD\cos(\phi_1-\phi_2-\theta_3+\theta_4)][A^4 + B^4 + C^4 + D^4 \\
& + 2A^2C^2 + 2B^2D^2 + 2A^2D^2 + 2B^2C^2 + 2A^2B^2 + 2C^2D^2 + 4A^2C^2\cos(2\phi_1-\theta_1-\theta_3) \\
& + 4B^2D^2\cos(2\phi_2-\theta_2-\theta_4) + 4A^2D^2\cos(\phi_1+\phi_2-\theta_1-\theta_4) + 4B^2C^2\cos(\phi_1+\phi_2-\theta_2-\theta_3) \\
& + 4A^2B^2\cos(\phi_1-\phi_2-\theta_1+\theta_2) + 4C^2D^2\cos(\phi_1-\phi_2-\theta_3+\theta_4) + 4ABCD\cos(2\phi_1-\theta_1-\theta_3) \\
& + 4ABCD\cos(2\phi_2-\theta_2-\theta_4) + 4ABCD\cos(\phi_1+\phi_2-\theta_1-\theta_4) + 4ABCD\cos(\phi_1+\phi_2-\theta_2-\theta_3) \\
& + 4ABCD\cos(\phi_1-\phi_2-\theta_1+\theta_2) + 4ABCD\cos(\phi_1-\phi_2-\theta_3+\theta_4)]N_{\hat{a}_{\text{in3}}}.
\end{aligned} \tag{A2}$$

For simplicity, the phase difference $(\theta_1-\theta_2, \theta_3-\theta_4, \phi_1-\phi_2)$ between fields with the same frequency inside FBNI is set to be equal, which can be realized by phase locking. In this way, the intensity noise of the measured field $\hat{b}_1$ can be simplified to

$$\begin{aligned}
\langle(\Delta\hat{N}_1)^2\rangle \approx\ & [2A^2C^2 + 2B^2D^2 + 4ABCD + 2A^2C^2\cos(2\phi_2-\theta_2-\theta_4) + 2B^2D^2\cos(2\phi_2-\theta_2-\theta_4) \\
& + 4ABCD\cos(2\phi_2-\theta_2-\theta_4)][A^4 + B^4 + C^4 + D^4 + 2A^2C^2 + 2B^2D^2 + 2A^2D^2 + 2B^2C^2 \\
& + 6A^2B^2 + 6C^2D^2 + 8ABCD + 4A^2C^2\cos(2\phi_2-\theta_2-\theta_4) + 4B^2D^2\cos(2\phi_2-\theta_2-\theta_4) \\
& + 4A^2D^2\cos(2\phi_2-\theta_2-\theta_4) + 4B^2C^2\cos(2\phi_2-\theta_2-\theta_4) + 16ABCD\cos(2\phi_2-\theta_2-\theta_4)]N_{\hat{a}_{\text{in3}}}.
\end{aligned} \tag{A3}$$

For convenience, $\varphi = 2\phi_2 - \theta_2 - \theta_4$ is defined as the total phase inside FBNI. Then, the intensity noise of the measured field $\hat{b}_1$ can be given by

$$\begin{aligned}
\langle(\Delta\hat{N}_1)^2\rangle \approx\ & (2A^2C^2 + 2B^2D^2 + 4ABCD + 2A^2C^2\cos\varphi + 2B^2D^2\cos\varphi + 4ABCD\cos\varphi)(A^4 + B^4 \\
& + C^4 + D^4 + 2A^2C^2 + 2B^2D^2 + 2A^2D^2 + 2B^2C^2 + 6A^2B^2 + 6C^2D^2 + 8ABCD \\
& + 4A^2C^2\cos\varphi + 4B^2D^2\cos\varphi + 4A^2D^2\cos\varphi + 4B^2C^2\cos\varphi + 16ABCD\cos\varphi)N_{\hat{a}_{\text{in3}}}.
\end{aligned} \tag{A4}$$

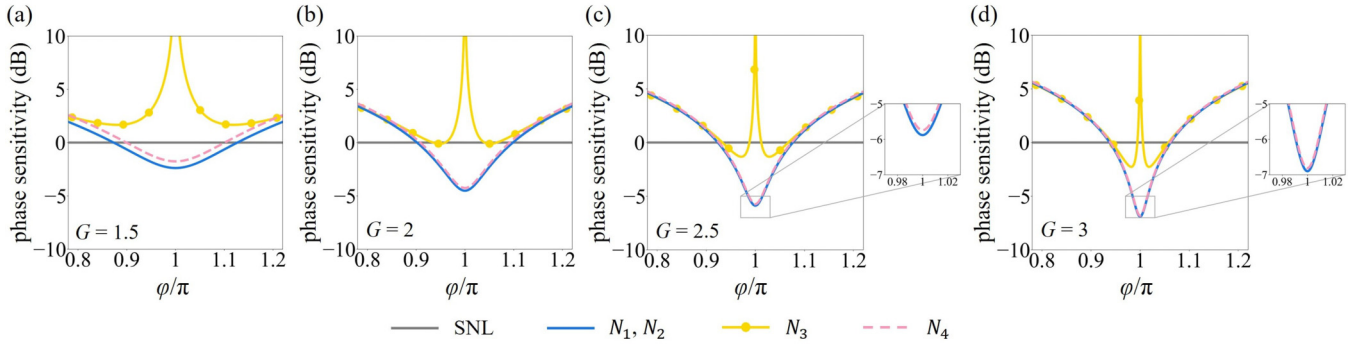

FIG. 5. The phase sensitivities of FBNI with photon number at a single output port and the corresponding SNL versus φ in the lossless case with the same internal photon number and $G_1 = G_2 = G$. When (a) $G = 1.5$, (b) $G = 2$, (c) $G = 2.5$, and (d) $G = 3$, the phase sensitivities of FBNI with photon number N_1 (N_2), N_3, and N_4 are denoted by blue solid, yellow dot, and pink dashed curves, respectively. The corresponding SNLs are denoted by gray straight lines.

When $G_1 = G_2 = G$, the corresponding phase sensitivity with photon number N_1 can be given by

$$\Delta\varphi_{N_1} = \frac{\sqrt{4\varepsilon(2G-1)^2(\cos\varphi+1)^2+(\cos\varphi+1)}}{\sqrt{\varepsilon N_s}|\sin\varphi|}, \tag{A5}$$

where $N_s = (2G-1)^2 N_{\hat{a}_{\text{in}3}}$ is the total internal photon number of the interferometer, and $\varepsilon = 2G(G-1)$. Similarly, the phase sensitivities of FBNI with photon number N_2, N_3, N_4 can be given by

$$\begin{aligned}
\Delta\varphi_{N_2} &= \frac{\sqrt{4\varepsilon(2G-1)^2(\cos\varphi+1)^2+(\cos\varphi+1)}}{\sqrt{\varepsilon N_s}|\sin\varphi|},\\
\Delta\varphi_{N_3} &= \frac{\sqrt{(2G-1)^2[\kappa\varepsilon(1+\varepsilon)(\cos\varphi+1)^2+2\varepsilon(3+5\varepsilon)(\cos\varphi+1)+1]}}{2\varepsilon(1+\varepsilon)|\sin\varphi|\sqrt{N_s}},\\
\Delta\varphi_{N_4} &= \frac{\sqrt{(2G-1)^2[4\varepsilon(2G-1)^2(\cos\varphi+1)^2+(\cos\varphi+1)]}}{\sqrt{2}\varepsilon|\sin\varphi|\sqrt{N_s}},
\end{aligned} \tag{A6}$$

where $\kappa = 16G(G-1)(2G-1)^2$. By comparing $\Delta\varphi_{N_1}$ and $\Delta\varphi_{N_2}$, it is observed that when $G_1 = G_2 = G$, the phase sensitivities with photon numbers N_1 and N_2 are equal.

In order to clearly compare the phase sensitivities of FBNI obtained by detecting photon number at a single port, these phase sensitivities versus φ are shown in Fig. 5 with the same internal photon number. As shown in Fig. 5, the blue solid, yellow dot, and pink dashed curves represent the phase sensitivities of FBNI with photon number N_1 (N_2), N_3, and N_4. The corresponding SNLs are denoted by gray straight lines. Within a phase region around π, the blue solid curves are always below the yellow dot and pink dashed curves for any value of G, as shown in Figs. 5(a)–5(d). In other words, the phase sensitivities of two conjugate output ports (N_1, N_2) of FBNI are better than those of probe output ports (N_3, N_4). As the intensity gain G increases from 1.5 to 3, the phase sensitivity of FBNI with photon number N_1 (N_2) is improved, as shown in Figs. 5(a)–5(d). When $G = 3$, the phase sensitivity of FBNI with photon number N_1 (N_2) is about 6.90 dB below the SNL, as obtained by comparing the minimum of the blue solid curve and gray straight line in Fig. 5(d).

We also calculate the phase sensitivities obtained from various combinations of photon numbers at any two output ports of the FBNI. The phase sensitivities of FBNI from combinations of photon numbers $N_1 - N_3$, $N_2 - N_3$, $N_3 - N_4$, $N_1 - N_4$, $N_2 - N_4$, $N_1 + N_3$, $N_2 + N_3$, $N_3 + N_4$, $N_1 + N_4$, $N_2 + N_4$, $N_1 + N_2$ can be given by

$$\begin{aligned}
\Delta\varphi_{N_1-N_3} &= \Delta\varphi_{N_2-N_3} = \frac{\sqrt{(2G-1)^2[\varepsilon(3+4\varepsilon)(\cos\varphi+1)+1]}}{\varepsilon|\sin\varphi|\sqrt{N_s}},\\
\Delta\varphi_{N_3-N_4} &= \frac{\sqrt{(2G-1)^2[6\varepsilon(2G-1)^2(\cos\varphi+1)+1]}}{2\varepsilon|\sin\varphi|\sqrt{N_s}},\\
\Delta\varphi_{N_1-N_4} &= \Delta\varphi_{N_2-N_4} = \frac{\sqrt{(2G-1)^2\varepsilon(1+4\varepsilon)(\cos\varphi+1)}}{\varepsilon|\sin\varphi|\sqrt{N_s}},\\
\Delta\varphi_{N_1+N_3} &= \Delta\varphi_{N_2+N_3} = \frac{\sqrt{(2G-1)^2[\varepsilon\kappa(3+4\varepsilon)(\cos\varphi+1)^2+\varepsilon(11+20\varepsilon)(\cos\varphi+1)+1]}}{\varepsilon\sqrt{N_s}(3+4\varepsilon)|\sin\varphi|},
\end{aligned}$$

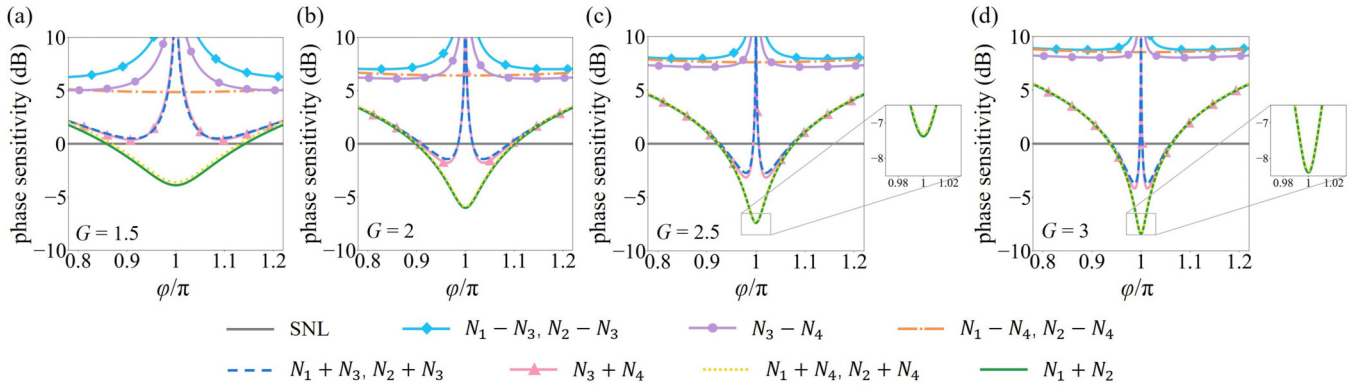

FIG. 6. The phase sensitivities of FBNI with various combinations of photon numbers at any two output ports and the corresponding SNL versus φ in the lossless case with the same internal photon number and $G_1 = G_2 = G$. When (a) $G = 1.5$, (b) $G = 2$, (c) $G = 2.5$, and (d) $G = 3$, the phase sensitivities of FBNI with photon number combinations $N_1 - N_3$ $(N_2 - N_3)$, $N_3 - N_4$, $N_1 - N_4$ $(N_2 - N_4)$, $N_1 + N_3$ $(N_2 + N_3)$, $N_3 + N_4$, $N_1 + N_4$ $(N_2 + N_4)$, and $N_1 + N_2$ are denoted by light blue diamond, purple dot, orange dash-dotted, dark blue dashed, pink triangle, yellow dotted, and dark green solid curves, respectively. The corresponding SNLs are denoted by gray straight lines.

$$\Delta\varphi_{N_3+N_4} = \frac{\sqrt{2\varepsilon\kappa(2G-1)^2(\cos\varphi+1)^2 + 6\varepsilon(2G-1)^2(\cos\varphi+1)+1}}{2\varepsilon(2G-1)|\sin\varphi|\sqrt{N_s}},$$
$$\Delta\varphi_{N_1+N_4} = \Delta\varphi_{N_2+N_4} = \frac{\sqrt{(2G-1)^2[\kappa(\cos\varphi+1)^2 + (\cos\varphi+1)]}}{\sqrt{\varepsilon(1+4\varepsilon)N_s}|\sin\varphi|},$$
$$\Delta\varphi_{N_1+N_2} = \frac{\sqrt{\kappa(\cos\varphi+1)^2 + (\cos\varphi+1)}}{\sqrt{2\varepsilon N_s}|\sin\varphi|}. \tag{A7}$$

As shown in Fig. 6, the phase sensitivities of FBNI with various photon number combinations $N_1 - N_3$ $(N_2 - N_3)$, $N_3 - N_4$, $N_1 - N_4$ $(N_2 - N_4)$, $N_1 + N_3$ $(N_2 + N_3)$, $N_3 + N_4$, $N_1 + N_4$ $(N_2 + N_4)$, and $N_1 + N_2$ versus φ are depicted by light blue diamond, purple dot, orange dash-dotted, dark blue dashed, pink triangle, yellow dotted, and dark green solid curves, respectively. The corresponding SNLs are denoted by gray straight lines. When $G_1 = G_2 = G$, photon numbers at two conjugate ports of FBNI are equal $(N_1 = N_2)$, that is, the denominator $|\partial\langle\hat{N}_1 - \hat{N}_2\rangle/\partial\varphi|$ is 0 and the phase sensitivities of FBNI with the photon number combination $N_1 - N_2$ cannot be plotted. Similarly, due to the equality of N_1 and N_2, swapping N_1 and N_2 in the photon number combinations does not change the corresponding phase sensitivity. So $\Delta\varphi_{N_1-N_3} = \Delta\varphi_{N_2-N_3}$, $\Delta\varphi_{N_1-N_4} = \Delta\varphi_{N_2-N_4}$, $\Delta\varphi_{N_1+N_3} = \Delta\varphi_{N_2+N_3}$, $\Delta\varphi_{N_1+N_4} = \Delta\varphi_{N_2+N_4}$ when $G_1 = G_2 = G$. The phase sensitivities of FBNI with photon number combinations $N_1 + N_4$ $(N_2 + N_4)$ and $N_1 + N_2$ are below those of the other combinations, as shown in Figs. 6(a)–6(d). Although the yellow dotted curves $[N_1 + N_4$ $(N_2 + N_4)]$ approach the dark green solid curves $(N_1 + N_2)$, a closer inspection of the zoomed-in plot in Fig. 6(d) reveals that the yellow dotted curves remain above the dark green solid curves. When $G = 3$ as shown in Fig. 6(d), the phase sensitivity obtained by detecting the photon number combination $N_1 + N_4$ $(N_2 + N_4)$ is about 8.36 dB below the SNL, whereas the phase sensitivity acquired from the photon number combination $N_1 + N_2$ is about 8.41 dB below the SNL. Therefore, for the phase sensitivity of FBNI obtained by joint measurement of two output ports, the optimal combination of photon numbers is $N_1 + N_2$.

Then, the phase sensitivities obtained from various combinations of photon numbers at any three output ports of the FBNI are calculated. The phase sensitivities of FBNI from photon number combinations $N_1 - N_3 + N_4$, $N_2 - N_3 + N_4$, $N_1 + N_2 - N_3$, $N_1 + N_3 - N_4$, $N_2 + N_3 - N_4$, $N_1 - N_2 - N_4$, $N_1 - N_2 + N_4$, $N_1 + N_2 + N_3$, $N_1 - N_3 - N_4$, $N_2 - N_3 - N_4$, $N_1 - N_2 - N_3$, $N_1 - N_2 + N_3$, $N_1 + N_3 + N_4$, $N_2 + N_3 + N_4$, $N_1 + N_2 - N_4$, $N_1 + N_2 + N_4$ can be given by

$$\Delta\varphi_{N_1-N_3+N_4} = \Delta\varphi_{N_2-N_3+N_4} = \frac{\sqrt{(2G-1)^2\{\kappa G[1+G(3+2\varepsilon-4G)](\cos\varphi+1)^2 + 3\varepsilon(2G-1)^2(\cos\varphi+1)+1\}}}{2G[1+G(3+2\varepsilon-4G)]|\sin\varphi|\sqrt{N_s}},$$
$$\Delta\varphi_{N_1+N_2-N_3} = \frac{\sqrt{(2G-1)^2[\kappa\varepsilon^2(\cos\varphi+1)^2 - 2\varepsilon^2(\cos\varphi+1)+1]}}{2\varepsilon^2|\sin\varphi|\sqrt{N_s}},$$
$$\Delta\varphi_{N_1+N_3-N_4} = \Delta\varphi_{N_2+N_3-N_4} = \frac{\sqrt{(2G-1)^2\{\kappa G(G-1)(3+2\varepsilon)(\cos\varphi+1)^2 + 11\varepsilon(2G-1)^2(\cos\varphi+1)+1\}}}{\varepsilon(3+2\varepsilon)|\sin\varphi|\sqrt{N_s}},$$

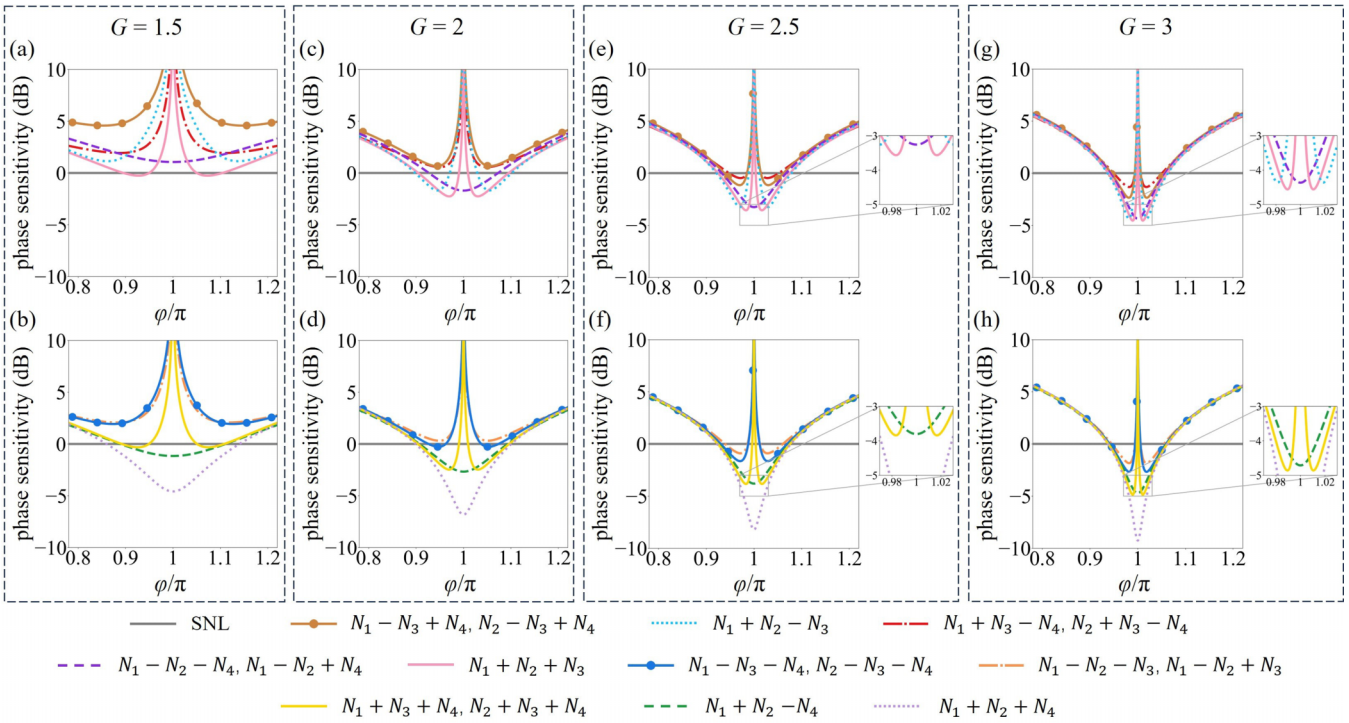

FIG. 7. The phase sensitivities of FBNI with various combinations of photon numbers at any three output ports and the corresponding SNL versus φ in the lossless case with the same internal photon number and $G_1 = G_2 = G$. When (a) $G = 1.5$, (c) $G = 2$, (e) $G = 2.5$, and (g) $G = 3$, the phase sensitivities of FBNI with photon number combinations $N_1 - N_3 + N_4$ ($N_2 - N_3 + N_4$), $N_1 + N_2 - N_3$, $N_1 + N_3 - N_4$ ($N_2 + N_3 - N_4$), $N_1 - N_2 - N_4$ ($N_1 - N_2 + N_4$), and $N_1 + N_2 + N_3$ are denoted by brown dot, light blue dotted, red dash-dotted, dark purple dashed, and pink solid curves, respectively. When (b) $G = 1.5$, (d) $G = 2$, (f) $G = 2.5$, and (h) $G = 3$, the phase sensitivities of FBNI with photon number combinations $N_1 - N_3 - N_4$ ($N_2 - N_3 - N_4$), $N_1 - N_2 - N_3$ ($N_1 - N_2 + N_3$), $N_1 + N_3 + N_4$ ($N_2 + N_3 + N_4$), $N_1 + N_2 - N_4$, and $N_1 + N_2 + N_4$ are denoted by dark blue dot, orange dash-dotted, yellow solid, dark green dashed, and light purple dotted curves, respectively. The corresponding SNLs are denoted by gray straight lines.

$$
\begin{aligned}
\Delta\varphi_{N_1-N_2-N_4} &= \Delta\varphi_{N_1-N_2+N_4} = \frac{\sqrt{(2G-1)^2\{2\varepsilon^3(2G-1)^2(\cos\varphi+1)^2+[G(G-1)+6G^2(G-1)^2](\cos\varphi+1)\}}}{\varepsilon^2|\sin\varphi|\sqrt{N_s}},\\
\Delta\varphi_{N_1+N_2+N_3} &= \frac{\sqrt{(2G-1)^2\{6\varepsilon\kappa[1+3G(G-1)](\cos\varphi+1)^2+4\varepsilon[4+15G(G-1)](\cos\varphi+1)+1\}}}{4\varepsilon[1+3G(G-1)]|\sin\varphi|\sqrt{N_s}},\\
\Delta\varphi_{N_1-N_3-N_4} &= \Delta\varphi_{N_2-N_3-N_4} = \frac{\sqrt{4\varepsilon^2(2G-1)^4(\cos\varphi+1)^2+3\varepsilon(2G-1)^2(\cos\varphi+1)+1}}{\varepsilon(2G-1)|\sin\varphi|\sqrt{N_s}},\\
\Delta\varphi_{N_1-N_2-N_3} &= \Delta\varphi_{N_1-N_2+N_3} = \frac{\sqrt{(2G-1)^2\{\varepsilon\kappa(1+\varepsilon)(\cos\varphi+1)^2+4\varepsilon[2+7G(G-1)](\cos\varphi+1)+1\}}}{2\varepsilon(1+\varepsilon)|\sin\varphi|\sqrt{N_s}},\\
\Delta\varphi_{N_1+N_3+N_4} &= \Delta\varphi_{N_2+N_3+N_4} = \frac{\sqrt{36\varepsilon^2(2G-1)^4(\cos\varphi+1)^2+11\varepsilon(2G-1)^2(\cos\varphi+1)+1}}{3\varepsilon(2G-1)|\sin\varphi|\sqrt{N_s}},\\
\Delta\varphi_{N_1+N_2-N_4} &= \frac{\sqrt{(2G-1)^2\{2\varepsilon^2(2G-1)^2(1+\varepsilon)(\cos\varphi+1)^2+[G(G-1)+6G^2(G-1)^2](\cos\varphi+1)\}}}{\varepsilon(1+\varepsilon)|\sin\varphi|\sqrt{N_s}},\\
\Delta\varphi_{N_1+N_2+N_4} &= \frac{\sqrt{(2G-1)^2[3\varepsilon\kappa(1+3\varepsilon)(\cos\varphi+1)^2+2(\varepsilon+3\varepsilon^2)(\cos\varphi+1)]}}{2\varepsilon(1+3\varepsilon)|\sin\varphi|\sqrt{N_s}}.
\end{aligned}
\tag{A8}
$$

There are multiple combinations of any three output ports. To reduce the overlapping of traces, the phase sensitivities for the same intensity gain are depicted in separate subplots, arranged vertically. As shown in Fig. 7, the phase sensitivities of FBNI with various photon number combinations $N_1 - N_3 + N_4$ ($N_2 - N_3 + N_4$), $N_1 + N_2 - N_3$, $N_1 + N_3 - N_4$ ($N_2 + N_3 - N_4$), $N_1 - N_2 - N_4$ ($N_1 - N_2 + N_4$), $N_1 + N_2 + N_3$, $N_1 - N_3 - N_4$ ($N_2 - N_3 - N_4$), $N_1 -$

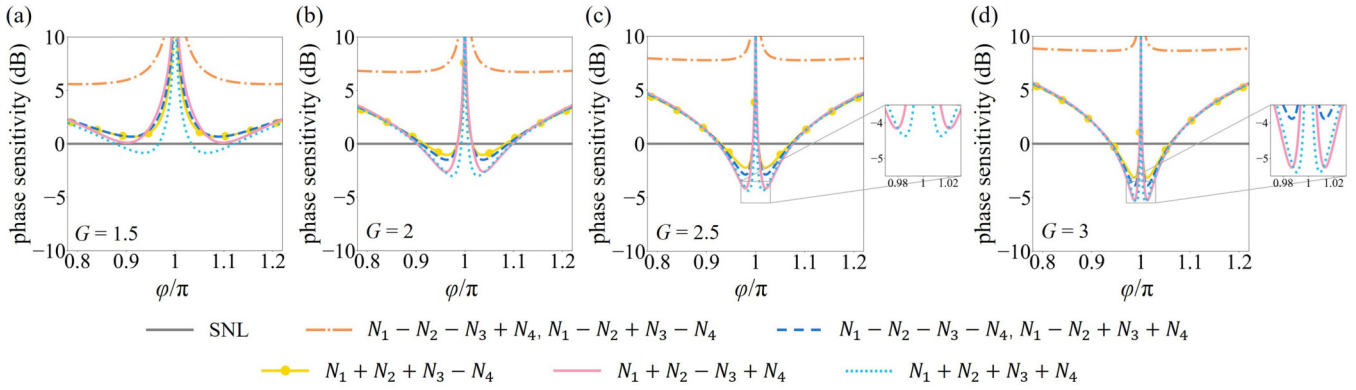

FIG. 8. The phase sensitivities of FBNI with various combinations of photon numbers at four output ports and the corresponding SNL versus φ in the lossless case with the same internal photon number and $G_1 = G_2 = G$. When (a) $G = 1.5$, (b) $G = 2$, (c) $G = 2.5$, and (d) $G = 3$, the phase sensitivities of FBNI with photon number combinations $N_1 - N_2 - N_3 + N_4$ ($N_1 - N_2 + N_3 - N_4$), $N_1 - N_2 - N_3 - N_4$ ($N_1 - N_2 + N_3 + N_4$), $N_1 + N_2 + N_3 - N_4$, $N_1 + N_2 - N_3 + N_4$, and $N_1 + N_2 + N_3 + N_4$ are denoted by orange dash-dotted, dark blue dashed, yellow dot, pink solid, and light blue dotted curves, respectively. The corresponding SNLs are denoted by gray straight lines.

$N_2 - N_3$ $(N_1 - N_2 + N_3)$, $N_1 + N_3 + N_4$ $(N_2 + N_3 + N_4)$, $N_1 + N_2 - N_4$, and $N_1 + N_2 + N_4$ versus φ are depicted by brown dot, light blue dotted, red dash-dotted, dark purple dashed, pink solid, dark blue dot, orange dash-dotted, yellow solid, dark green dashed, and light purple dotted curves, respectively. The corresponding SNLs are denoted by gray straight lines. Similar to the case of two-port combinations, N_1 and N_2 can also be swapped in the case of three-port combinations. This is also the reason why $\Delta\varphi_{N_1-N_2-N_4} = \Delta\varphi_{N_1-N_2+N_4}$, $\Delta\varphi_{N_1-N_2-N_3} = \Delta\varphi_{N_1-N_2+N_3}$. In Figs. 7(a), 7(c), 7(e), and 7(g), the optimal phase sensitivities are derived from photon number combination $N_1 + N_2 + N_3$ (pink solid curves). As shown in Fig. 7(g), the phase sensitivities of FBNI with photon number combination $N_1 + N_2 + N_3$ can beat the SNL 4.56 dB at optimal phase points when $G = 3$. In Figs. 7(b), 7(d), 7(f), and 7(h), the phase sensitivities of FBNI derived from the photon number combination $N_1 + N_2 + N_4$ (light purple dotted curves) show a clear superiority over those obtained from other combinations. As shown in Fig. 7(h), when $G = 3$, the best phase sensitivity in light purple dotted curve ($N_1 + N_2 + N_4$) is approximately 9.26 dB below the gray straight line (SNL). For the same intensity gain $G = 3$, the best phase sensitivity achieved from photon number combination $N_1 + N_2 + N_4$ (9.26 dB below the SNL) is significantly better than that achieved from photon number combination $N_1 + N_2 + N_3$ (4.56 dB below the SNL). Hence, for the phase sensitivity of FBNI obtained by a joint measurement of three output ports, the optimal combination of photon numbers is $N_1 + N_2 + N_4$.

In addition, the phase sensitivities obtained from various combinations of photon numbers at four output ports of the FBNI are also calculated. The phase sensitivities of FBNI with photon number combinations $N_1 - N_2 - N_3 + N_4$, $N_1 - N_2 + N_3 - N_4$, $N_1 - N_2 - N_3 - N_4$, $N_1 - N_2 + N_3 + N_4$, $N_1 + N_2 + N_3 - N_4$, $N_1 + N_2 - N_3 + N_4$, $N_1 + N_2 + N_3 + N_4$ can be given by

$$\begin{aligned}
\Delta\varphi_{N_1-N_2-N_3+N_4} &= \Delta\varphi_{N_1-N_2+N_3-N_4} = \frac{\sqrt{(2G-1)^2[\kappa(\cos\varphi+1)+1]}}{2\varepsilon|\sin\varphi|\sqrt{N_s}},\\
\Delta\varphi_{N_1-N_2-N_3-N_4} &= \Delta\varphi_{N_1-N_2+N_3+N_4} = \frac{\kappa(\cos\varphi+1)+2}{4\varepsilon(2G-1)|\sin\varphi|\sqrt{N_s}},\\
\Delta\varphi_{N_1+N_2+N_3-N_4} &= \frac{\sqrt{(2G-1)^2[4\varepsilon\kappa(1+\varepsilon)(\cos\varphi+1)^2+2\kappa(\cos\varphi+1)+1]}}{4\varepsilon(1+\varepsilon)|\sin\varphi|\sqrt{N_s}},\\
\Delta\varphi_{N_1+N_2-N_3+N_4} &= \frac{\sqrt{(2G-1)^2[4\varepsilon^2\kappa(\cos\varphi+1)^2+1]}}{4\varepsilon^2|\sin\varphi|\sqrt{N_s}},\\
\Delta\varphi_{N_1+N_2+N_3+N_4} &= \frac{\kappa(\cos\varphi+1)+1}{4\varepsilon(2G-1)|\sin\varphi|\sqrt{N_s}}.
\end{aligned} \tag{A9}$$

As shown in Fig. 8, the phase sensitivities of FBNI with photon number combinations $N_1 - N_2 - N_3 + N_4$ ($N_1 - N_2 + N_3 - N_4$), $N_1 - N_2 - N_3 - N_4$ $(N_1 - N_2 + N_3 + N_4)$, $N_1 + N_2 + N_3 - N_4$, $N_1 + N_2 - N_3 + N_4$, and $N_1 + N_2 + N_3 + N_4$ versus φ are depicted by orange dash-dotted, dark blue dashed, yellow dot, pink solid, and light blue dotted curves, respectively. The corresponding SNLs are denoted by gray straight lines. For the photon number combination $N_1 + N_2 -$

$N_3 - N_4$, the corresponding numerator $\sqrt{\frac{N_s}{(2G-1)^2}}$ and denominator 0 are both independent of the phase φ, making it impossible to obtain phase sensitivity. Figures 8(a)–8(d) illustrate that the phase sensitivities of FBNI, obtained from the photon number combinations $N_1 + N_2 - N_3 + N_4$ (pink solid curves) and $N_1 + N_2 + N_3 + N_4$ (light blue dotted curves), are better than those from other combinations for any value of G. Specifically, when $G = 3$ as shown in Fig. 8(d), the best phase sensitivities of FBNI with photon number combinations $N_1 + N_2 - N_3 + N_4$ and $N_1 + N_2 + N_3 + N_4$ are approximately 5.26 dB and 5.40 dB below the SNL, respectively. In other words, for the phase sensitivities of FBNI obtained by joint measurement of four output ports, the optimal combination of photon numbers is $N_1 + N_2 + N_3 + N_4$.

APPENDIX B: EFFECT OF LOSSES ON FBNI

In order to characterize the effect of losses on the phase sensitivity of FBNI, we regard the output field after losses as a combination of the input field and vacuum field on a beam splitter [41]. Therefore, the input-output relations of FBNI can be expressed as

$$\begin{aligned}\hat{b}'_{\mathrm{FBNI}} = {} & [\sqrt{1-\eta_1}A^2 e^{i\theta_1} + \sqrt{1-\eta_2}B^2 e^{i(\phi_1-\phi_2+\theta_2)} + \sqrt{1-\eta_3}C^2 e^{i(2\phi_1-\theta_3)} + \sqrt{1-\eta_4}D^2 e^{i(\phi_1+\phi_2-\theta_4)}]\hat{a}_{\mathrm{in1}} \\ & + [\sqrt{1-\eta_1}ABe^{i\theta_1} + \sqrt{1-\eta_2}ABe^{i(\phi_1-\phi_2+\theta_2)} + \sqrt{1-\eta_3}CDe^{i(2\phi_1-\theta_3)} + \sqrt{1-\eta_4}CDe^{i(\phi_1+\phi_2-\theta_4)}]\hat{a}_{\mathrm{in2}} \\ & + [\sqrt{1-\eta_1}ACe^{i\theta_1} + \sqrt{1-\eta_2}BDe^{i(\phi_1-\phi_2+\theta_2)} + \sqrt{1-\eta_3}ACe^{i(2\phi_1-\theta_3)} + \sqrt{1-\eta_4}BDe^{i(\phi_1+\phi_2-\theta_4)}]\hat{a}^\dagger_{\mathrm{in3}} \\ & + [\sqrt{1-\eta_1}ADe^{i\theta_1} + \sqrt{1-\eta_2}BCe^{i(\phi_1-\phi_2+\theta_2)} + \sqrt{1-\eta_3}BCe^{i(2\phi_1-\theta_3)} + \sqrt{1-\eta_4}ADe^{i(\phi_1+\phi_2-\theta_4)}]\hat{a}^\dagger_{\mathrm{in4}} \\ & + A\sqrt{\eta_1}e^{i\theta_1}\hat{v}_1 + B\sqrt{\eta_2}e^{i(\phi_1-\phi_2+\theta_2)}\hat{v}_2 + C\sqrt{\eta_3}e^{i(2\phi_1-\theta_3)}\hat{v}^\dagger_3 + D\sqrt{\eta_4}e^{i(\phi_1+\phi_2-\theta_4)}\hat{v}^\dagger_4, \end{aligned} \tag{B1}$$

where η_l (l=1, 2, 3, and 4) denotes the loss ratio of FBNI on each arm and the annihilation operator $\hat{v}_l$ denotes the corresponding vacuum field. For simplicity, we consider the loss ratios of FBNI as η, namely, $\eta_1 = \eta_2 = \eta_3 = \eta_4 = \eta$. Then, the phase sensitivity of FBNI in the case of considering the losses can be given by

$$\Delta\varphi'_{\mathrm{FBNI}} = \sqrt{\frac{(2G-1)^2\{8\varepsilon(1-\eta)(1+3\varepsilon)[6+3G^3\eta^2(18G^3-60G^2+77G-47)+4G(\sigma-7)+8G^2(8-5\sigma)]\cos^2\frac{\varphi}{2}+2-\eta+2\varepsilon[\eta+3+3G\eta(6G-5)]\}}{8\sin^2\frac{\varphi}{2}\varepsilon(1+3\varepsilon)^2N_s}}, \tag{B2}$$

where $\varepsilon = 2G(G-1)$, and $\sigma = (1-\eta)(\eta+1)$. At the optimal phase point $\varphi = \pi$, Eq. (B2) can be represented by

$$\Delta\varphi'_{\mathrm{FBNI}} = \sqrt{\frac{(2G-1)^2\{2-\eta+2\varepsilon[\eta+3+3G\eta(6G-5)]\}}{8\varepsilon(1+3\varepsilon)^2N_s}}. \tag{B3}$$

[1] M. Born, E. Wolf, A. B. Bhatia, P. C. Clemmow, D. Gabor, A. R. Stokes, A. M. Taylor, P. A. Wayman, and W. L. Wilcock, *Principles of Optics* (Cambridge University Press, Cambridge, 1999).

[2] A. Lenef, T. D. Hammond, E. T. Smith, M. S. Chapman, R. A. Rubenstein, and D. E. Pritchard, Rotation sensing with an atom interferometer, Phys. Rev. Lett. **78**, 760 (1997).

[3] C. M. Caves, Quantum-mechanical noise in an interferometer, Phys. Rev. D **23**, 1693 (1981).

[4] S. L. Braunstein, Quantum limits on precision measurements of phase, Phys. Rev. Lett. **69**, 3598 (1992).

[5] V. Giovannetti, S. Lloyd, and L. Maccone, Quantum metrology, Phys. Rev. Lett. **96**, 010401 (2006).

[6] V. Giovannetti, S. Lloyd, and L. Maccone, Advances in quantum metrology, Nature Photon. **5**, 222 (2011).

[7] L. Pezzè, A. Smerzi, M. K. Oberthaler, R. Schmied, and P. Treutlein, Quantum metrology with nonclassical states of atomic ensembles, Rev. Mod. Phys. **90**, 035005 (2018).

[8] M. Xiao, L.-A. Wu, and H. J. Kimble, Precision measurement beyond the shot-noise limit, Phys. Rev. Lett. **59**, 278 (1987).

[9] K. Goda, O. Miyakawa, E. E. Mikhailov, S. Saraf, R. Adhikari, K. McKenzie, R. Ward, S. Vass, A. J. Weinstein, and N. Mavalvala, A quantum-enhanced prototype gravitational-wave detector, Nature Phys. **4**, 472 (2008).

[10] L. Pezzé, A. Smerzi, Mach-Zehnder interferometry at the Heisenberg limit with coherent and squeezed-vacuum light, Phys. Rev. Lett. **100**, 073601 (2008).

[11] The LIGO Scientific Collaboration, A gravitational wave observatory operating beyond the quantum shot-noise limit, Nature Phys. **7**, 962 (2011).

[12] M. J. Holland and K. Burnett, Interferometric detection of optical phase shifts at the Heisenberg limit, Phys. Rev. Lett. **71**, 1355 (1993).

[13] J. J. Bollinger, W. M. Itano, D. J. Wineland, and D. J. Heinzen, Optimal frequency measurements with maximally correlated states, Phys. Rev. A **54**, R4649 (1996).

[14] J. P. Dowling, Quantum optical metrology–the lowdown on high-N00N states, Contemp. Phys. **49**, 125 (2008).

[15] M. Tse *et al.*, Quantum-enhanced advanced LIGO detectors in the era of gravitational-wave astronomy, Phys. Rev. Lett. **123**, 231107 (2019).

[16] J. Lough, E. Schreiber, F. Bergamin, H. Grote, M. Mehmet, H. Vahlbruch, C. Affeldt, M. Brinkmann, A. Bisht, V. Kringel *et al.*, First demonstration of 6 dB quantum noise reduction in a kilometer scale gravitational wave observatory, Phys. Rev. Lett. **126**, 041102 (2021).

[17] P. Grangier, R. E. Slusher, B. Yurke, and A. LaPorta, Squeezed-light-enhanced polarization interferometer, Phys. Rev. Lett. **59**, 2153 (1987).

[18] P. M. Anisimov, G. M. Raterman, A. Chiruvelli, W. N. Plick, S. D. Huver, H. Lee, and J. P. Dowling, Quantum metrology with two-mode squeezed vacuum: Parity detection beats the Heisenberg limit, Phys. Rev. Lett. **104**, 103602 (2010).

[19] D. Li, B. T. Gard, Y. Gao, C.-H. Yuan, W. Zhang, H. Lee, and J. P. Dowling, Phase sensitivity at the Heisenberg limit in an SU(1,1) interferometer via parity detection, Phys. Rev. A **94**, 063840 (2016).

[20] J. Heinze, K. Danzmann, B. Willke, and H. Vahlbruch, 10 dB quantum-enhanced michelson interferometer with balanced homodyne detection, Phys. Rev. Lett. **129**, 031101 (2022).

[21] S. Ataman, A. Preda, and R. Ionicioiu, Phase sensitivity of a Mach-Zehnder interferometer with single-intensity and difference-intensity detection, Phys. Rev. A **98**, 043856 (2018).

[22] L. Zehnder, Ein neuer Interferenzrefraktor, Z. Instrumentenkd. **11**, 275 (1891).

[23] L. Mach, Ueber einen Interferenzrefraktor, Z. Instrumentenkd. **12**, 89 (1892).

[24] B. Yurke, S. L. McCall, and J. R. Klauder, SU(2) and SU(1,1) interferometers, Phys. Rev. A **33**, 4033 (1986).

[25] J. Jing, C. Liu, Z. Zhou, Z. Y. Ou, and W. Zhang, Realization of a nonlinear interferometer with parametric amplifiers, Appl. Phys. Lett. **99**, 011110 (2011).

[26] F. Hudelist, J. Kong, C. Liu, J. Jing, Z. Y. Ou, and W. Zhang, Quantum metrology with parametric amplifier-based photon correlation interferometers, Nature Commun. **5**, 3049 (2014).

[27] B. E. Anderson, B. L. Schmittberger, P. Gupta, K. M. Jones, and P. D. Lett, Optimal phase measurements with bright- and vacuum-seeded SU(1,1) interferometers, Phys. Rev. A **95**, 063843 (2017).

[28] B. E. Anderson, P. Gupta, B. L. Schmittberger, T. Horrom, C. Hermann-Avigliano, K. M. Jones, and P. D. Lett, Phase sensing beyond the standard quantum limit with a variation on the SU(1,1) interferometer, Optica **4**, 752 (2017).

[29] S. S. Szigeti, R. J. Lewis-Swan, and S. A. Haine, Pumped-Up SU(1,1) interferometry, Phys. Rev. Lett. **118**, 150401 (2017).

[30] M. Manceau, G. Leuchs, F. Khalili, and M. Chekhova, Detection loss tolerant supersensitive phase measurement with an SU(1,1) interferometer, Phys. Rev. Lett. **119**, 223604 (2017).

[31] C. M. Caves, Reframing SU(1,1) Interferometry, Adv. Quantum Technol. **3**, 1900138 (2020).

[32] S. Liu, Y. Lou, J. Xin, and J. Jing, Quantum enhancement of phase sensitivity for the bright-seeded SU(1,1) interferometer with direct intensity detection, Phys. Rev. Appl. **10**, 064046 (2018).

[33] J.-D. Zhang, C. You, C. Li, and S. Wang, Phase sensitivity approaching the quantum Cramér-Rao bound in a modified SU(1,1) interferometer, Phys. Rev. A **103**, 032617 (2021).

[34] S. Chang, W. Ye, H. Zhang, L. Hu, J. Huang, and S. Liu, Improvement of phase sensitivity in an SU(1,1) interferometer via a phase shift induced by a Kerr medium, Phys. Rev. A **105**, 033704 (2022).

[35] R. Tang, J. Lasri, P. S. Devgan, V. Grigoryan, P. Kumar, and M. Vasilyev, Gain characteristics of a frequency nondegenerate phase-sensitive fiber-optic parametric amplifier with phase self-stabilized input, Opt. Express **13**, 10483 (2005).

[36] C. F. McCormick, V. Boyer, E. Arimonda, and P. D. Lett, Strong relative intensity squeezing by four-wave mixing in rubidium vapor, Opt. Lett. **32**, 178 (2007).

[37] V. Boyer, A. M. Marino, R. C. Pooser, and P. D. Lett, Entangled images from four-wave mixing, Science **321**, 544 (2008).

[38] W. Wang, K. Zhang, and J. Jing, Large-scale quantum network over 66 orbital angular momentum optical modes, Phys. Rev. Lett. **125**, 140501 (2020).

[39] K. Zhang, W. Wang, S. Liu, X. Pan, J. Du, Y. Lou, S. Yu, S. Lv, N. Treps, C. Fabre, and J. Jing, Reconfigurable hexapartite entanglement by spatially multiplexed four-wave mixing processes, Phys. Rev. Lett. **124**, 090501 (2020).

[40] S. Ataman, Single- versus two-parameter Fisher information in quantum interferometry, Phys. Rev. A **102**, 013704 (2020).

[41] H.-A. Bachor and T. C. Ralph, *A Guide to Experiments in Quantum Optics* (Wiley-VCH, Weinheim, 2004).

[42] A. M. Marino, N. V. Corzo Trejo, and P. D. Lett, Effect of losses on the performance of an SU(1,1) interferometer, Phys. Rev. A **86**, 023844 (2012).

[43] C. W. Helstrom, *Quantum Detection and Estimation Theory* (Academic Press, New York, 1976).